

Geophysical Research Letters®



RESEARCH LETTER

10.1029/2024GL110318

Turbulent Vertical Velocities in Labrador Sea Convection

L. Clément¹ , L. Merckelbach², and E. Frajka-Williams³ 

¹National Oceanography Centre, Southampton, UK, ²Institute of Coastal Research, Helmholtz-Zentrum Hereon, Geesthacht, Germany, ³Universität Hamburg, Hamburg, Germany

Key Points:

- Vertical velocity during deep ocean convection follows scalings from the atmospheric boundary layer under wind and buoyancy forcing
- Vertical velocity help identify convective plumes with a horizontal scale of 620 m and a downward velocity magnitude up to 4.6 cm s⁻¹
- Positive vertical buoyancy flux occurs during convection, caused by atmospheric cooling and then by freshwater flux during restratification

Supporting Information:

Supporting Information may be found in the online version of this article.

Correspondence to:

L. Clément,
l.clement@noc.ac.uk

Citation:

Clément, L., Merckelbach, L., & Frajka-Williams, E. (2024). Turbulent vertical velocities in Labrador Sea convection. *Geophysical Research Letters*, 51, e2024GL110318. <https://doi.org/10.1029/2024GL110318>

Received 16 MAY 2024

Accepted 27 OCT 2024

Abstract Turbulent vertical velocity measurements are scarce in regions prone to convection such as the Labrador Sea, which hinders our understanding of deep convection dynamics. Vertical velocity, w , is retrieved from wintertime glider deployments in the convective region. From w , downward convective plumes of dense waters are identified. These plumes only cover a small fraction of the convective area. Throughout the convective area, the standard deviation of w agrees with scaling relations for the atmospheric surface and boundary layers. It initially depends on surface buoyancy loss in winter, and later, on wind stress after mid-March. Both periods are characterized by positive turbulent vertical buoyancy flux. During convective periods in winter, the positive buoyancy flux is mostly forced by surface heat loss. After mid-March, when buoyancy loss to the atmosphere is reduced, the positive buoyancy flux results from a restratifying upward freshwater flux, potentially of lateral origins and without much atmospheric influence.

Plain Language Summary Deep convection is an essential component of our climate system as it uptakes and redistributes atmospheric properties, such as anthropogenic carbon and oxygen, into the abyssal ocean. Intense ocean heat loss to the atmosphere in winter triggers convection, resulting in kilometer-sized plumes with high downward vertical velocities and deep mixed layer depth. These plumes remain challenging to observe and parameterize in climate models. Here we show that autonomous vehicles (gliders) can sample dense downwelling plumes in the Labrador Sea. Gliders sampled a positive vertical buoyancy flux that depicts downwelling of dense water parcels and upwelling of light water parcels during convection, and that compensates a buoyancy loss from the ocean to the atmosphere. At the end of convection, an observed freshwater import produces a similar buoyancy flux unmatched by the surface flux. This flux adds buoyancy and shoals the mixed layer. Additional measurements from sufficiently long glider deployments like these ones could potentially allow us to establish a crucial link between deep water formation and an expected increase in freshwater fluxes from Arctic and Greenland sources.

1. Introduction

Through the ventilation of the deep ocean, convection mitigates the atmospheric accumulation of anthropogenic carbon dioxide. Climate models struggle to represent oceanic convection (F. Li et al., 2019) due to the wide range of scales involved in its development and cessation (Gascard & Clarke, 1983). One of the few regions where deep convection can occur is the Labrador Sea, where a cyclonic gyre with isopycnal doming preconditions the region to deep convection. Subsequently, the buoyant boundary currents bring buoyancy to the central Labrador Sea, contributing to the weakening of convection. After intense surface heat loss, overturning cells develop as kilometer-sized plumes with strong vertical velocities; these upwell buoyant water parcels and downwell less buoyant ones, mixing water properties. Convective plumes can be detected from vertical water velocities w (Margirier et al., 2017) estimated from gliders (Frajka-Williams et al., 2011; Merckelbach et al., 2010) or moored measurements (Schott et al., 1996). In this study, Labrador Sea convective plumes are identified and characterized from glider deployments.

Turbulent processes in the oceanic boundary layer (BL) result from surface buoyancy loss, winds, and waves. A lack of turbulent flux measurements in harsh convective environments limits the development of BL parameterizations (Large et al., 1994). These parameterizations rely on similarity theories developed for atmospheric boundary layers, where direct measurements of turbulent fluxes are more easily attainable. Similarity theories relate mean profiles of water properties with turbulent fluxes, obtained only from surface fluxes and subsurface shear and stratification profiles (Businger et al., 1971; Wyngaard et al., 1971). To study BL turbulence, microstructure profiles (Lombardo & Gregg, 1989) can be complemented by vertical kinetic energy, inferred from w (D'Asaro, 2001; Zheng, 2023). In a convective environment with surface heat loss (Figure 1a), a thermal

© 2024. The Author(s).

This is an open access article under the terms of the [Creative Commons Attribution License](https://creativecommons.org/licenses/by/4.0/), which permits use, distribution and reproduction in any medium, provided the original work is properly cited.

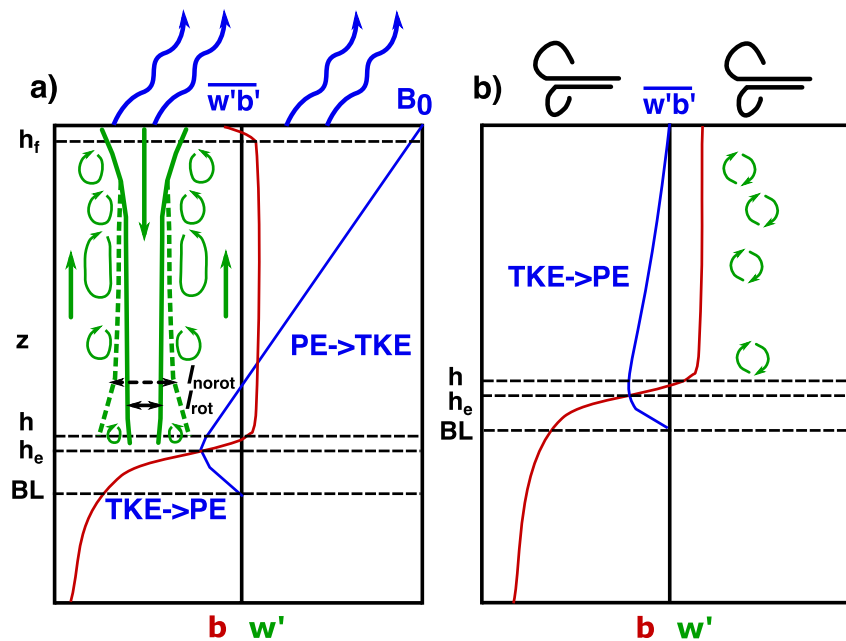


Figure 1. Ocean boundary layer (BL), entrainment depth (h_e), mixed layer depth (h), and surface layer (h_f) under (a) convective surface buoyancy loss and (b) wind-driven boundary layer. Vertical velocity anomalies (w' , green), buoyancy profile (b , red), and vertical buoyancy flux ($\overline{w'b'}$, blue) for (a) downward convective plumes and (b) wind-driven mixing. Earth's rotation can affect the convective plumes and restrict their lateral extent (green lines, l_{rot}) or has no effect on the plumes (dashed green lines, l_{norot}).

boundary layer appears with 3D turbulence. Below a critical depth, 3D turbulence becomes geostrophically controlled by planetary rotation and grows into quasi-2D and downward propagating vortices (Maxworthy & Narimousa, 1994). At the convective front around the plumes, eddies develop and export recently convected water masses. The efficiency of this water mass export depends on the eddy size, which, along with plume size, decreases with stronger rotational influence. Here, using data from glider deployments in a region of deep convection allows us to test the drivers of the w variability and the rotational influence on plumes.

Upward vertical buoyancy fluxes result from gravitational instabilities under convection but also from restratifying submesoscale and mesoscale processes. Buoyancy flux measurements are scarce in the open ocean BL because of the difficulty to sample small oceanic w with stable moored sensors. This challenge has been overcome with tethered sensors below drifting ice (McPhee, 1992) or with autonomous vehicles (Hayes & Morison, 2002). Because sampled subsurface buoyancy flux is still lacking in the ocean, bulk (Niiler & Krauss, 1977) or depth-dependent (Large et al., 1994; Reichl & Hallberg, 2018) oceanic mixed layer (ML) parameterizations rely on atmospheric buoyancy flux (Caughey & Palmer, 1979; Stull, 1976) at the entrainment depth (Figure 1a). Furthermore, buoyancy flux in a convective regime can be separated into a diffusive and downgradient buoyancy flux, which acts onto vertical gradients close to zero in a convective ML, and an advective and countergradient flux, parameterized from atmospheric convective updrafts (Giordani et al., 2020; Siebesma et al., 2007). Identifying Labrador Sea plumes should enable us to estimate the latter advective flux in a severe convective environment, and buoyancy flux can be estimated at the entrainment depth from gliders.

Labrador Sea restratification results from the added buoyancy by surface heating, and by the import of buoyancy from warm (Gelderloos et al., 2011; Lilly et al., 2003) or fresh (Clément et al., 2023; Rykova et al., 2009) eddies. The balance of temperature versus salinity in restratification remains uncertain in observations and models, but in a warming world with increased freshwater fluxes from the Arctic and Greenland, the effect on convection may differ depending on this balance. To investigate Labrador Sea convective plumes (Section 3.1) and the w scalings (Section 3.2), three gliders were deployed in the Labrador Sea (Figure S1 in Supporting Information S1) in winter (2020 and 2022). From w , temperature, and salinity profiles, we then estimate vertical buoyancy flux in the mixed layer both during convection and restratification (Section 3.3).

Table 1
Boundary Layer Scalings (Text S1 in Supporting Information S1)

	Turbulence scale	Non-dimensional parameter	Stable surface buoyancy ($B_0 < 0$)	Unstable surface buoyancy ($B_0 > 0$)
Surface layer SL (0%–10% of BL)	z	z/L with $L = -u_*^3/\kappa B_0$ $\kappa \approx 0.4$ $u_* = \sqrt{(\tau/\rho_0)}$ τ : wind stress	$z/L < 0$ with $L > 0$ $\sigma_w/u_* = 1$ (Figure 3a) (Wilson, 2008)	$z/L > 0$ with $L < 0$ $\sigma_w/u_* = (1 + 4.5z/L)^{1/3}$ (Figure 3b) (Wyngaard et al., 1971) • $z/L \ll 1$, forced convection (winds dominated): $\sigma_w/u_* \rightarrow 1$ • $z/L \gg 1$, Free convection (buoyancy dominated): $\sigma_w/u_* \sim (z/L)^{1/3}$
Mixed layer ML (0%–80% of BL)	$l_{rot} \sim (B_0/f^3)^{1/2}$ $l_{norot} \sim h$ (Jones & Marshall, 1993)	$Ro^* = (B_0/f^3 h^2)^{1/2}$ z/h	$\sigma_w^2/u_*^2 = 1.96(1 - z/h)^{3/2}$ (Figure 3c) (Nieuwstadt, 1984)	• $Ro^* < 0.29$, rotational convection: $w_* \rightarrow w_*^{rot} \sim (B_0/f)^{1/2}$ (Figure 3d): $\sigma_w^2/w_*^2 = 1$ (Mironov et al., 2000) • $Ro^* > 0.29$, non-rotational convection: $w_* \rightarrow w_*^{norot} \sim (B_0 h)^{1/3}$ (Figure 3e): $\sigma_w^2/w_*^2 = 1.8(z/h)^{5/3}(1 - 0.8z/h)^2$ (Lenschow et al., 1980)

2. Data and Methods

Three Slocum gliders sampled the Labrador Sea in the winter-spring seasons by profiling to 1,000 m. Gliders 398 and 409 were deployed in December 2021 from Qaqortoq, southwest Greenland, and retrieved in late May 2022 onboard the RV *Celtic Explorer*. Glider 398 made southwest-northeast ~ 10 -km sections in the convective region around 56°N 53°W . Glider 409 also made sections around the convective region but further north, around 58°N 55°W (Figure S1 in Supporting Information S1). The third glider Pearldiver sampled the center of the deep convective region around 57°N 52°W from January–May 2020, as described in Clément et al. (2023). Pearldiver sampled temperature (Θ) and salinity (S) at 20 s intervals, whereas the other two gliders sampled at 2 s intervals. In this study, we focus on data collected from mid-January (at the onset of convection, for 398 and Pearldiver) or late January (when the glider arrived at the convective site, for 409) until the last week of March (restratification). During these ~ 2.5 -month periods, the three gliders sampled the convective region, where the mixed layer depth deepens to more than 200 m in winter and shoals to 50 m during the last 2 weeks of March. The gliders traveled horizontally and vertically at a speed of 0.2 and 0.1 m s⁻¹, respectively.

Vertical water velocity, w , is estimated from glider data by subtracting a modeled glider flight speed, w_g , from a measured glider vertical velocity, w_m (Frajka-Williams et al., 2011; Merkelbach et al., 2010), $w = w_m - w_g$. Using the pressure sensor, w_m is the time derivative of the glider vertical position. A quasi-steady dynamical model for flight in still-water predicts w_g over timescales longer than 1 min by utilizing the balance between gravity, buoyancy, lift and drag forces. The computed water velocities have an accuracy of ~ 0.5 cm s⁻¹ and do not contain a signal due to (deep water) surface waves (Merkelbach & Carpenter, 2021). Values for w , collected in the top and bottom 20 m of each profile were not included in the analysis, as here the assumption of steady-state flight might not be valid due to changes in pitch and buoyancy drive. Following Margirier et al. (2017), convected plumes are detected by first identifying convective days during which $|w| > 2$ cm s⁻¹ for 10% of the day. Plumes are then detected when the 2-min running mean $|w|$ is above 2 cm s⁻¹ for a distance of at least 150 m.

Vertical velocity anomalies, w' , are estimated relative to a 60-min average, which roughly corresponds to the plume timescale (Sections 3.1), when calculating the standard deviation of the vertical velocity, $\sigma_w = (\overline{w'^2})^{1/2}$, in Sections 3.1 and 3.2. To estimate the buoyancy flux, $w'b'$, in Section 3.3, the averaged buoyancy is calculated by taking the mean over 1-day periods in z/h space, from which the anomaly b' and $w'b'$ are calculated, assuming that the average of w over these periods is zero. Although the buoyancy flux sampling interval approaches one minute when using a flight model, McPhee (1992) previously estimated that a resolved turbulent heat flux was reduced by only 10%–20% when low-pass filtering 1-s time series to 30 s. Below, overbars represent temporal average distinguishing between periods of different buoyancy forcing or convective scalings (defined from Ro^* , Table 1) as in Figure 3, or separating the periods of convection from restratification as in Figure 4. The natural

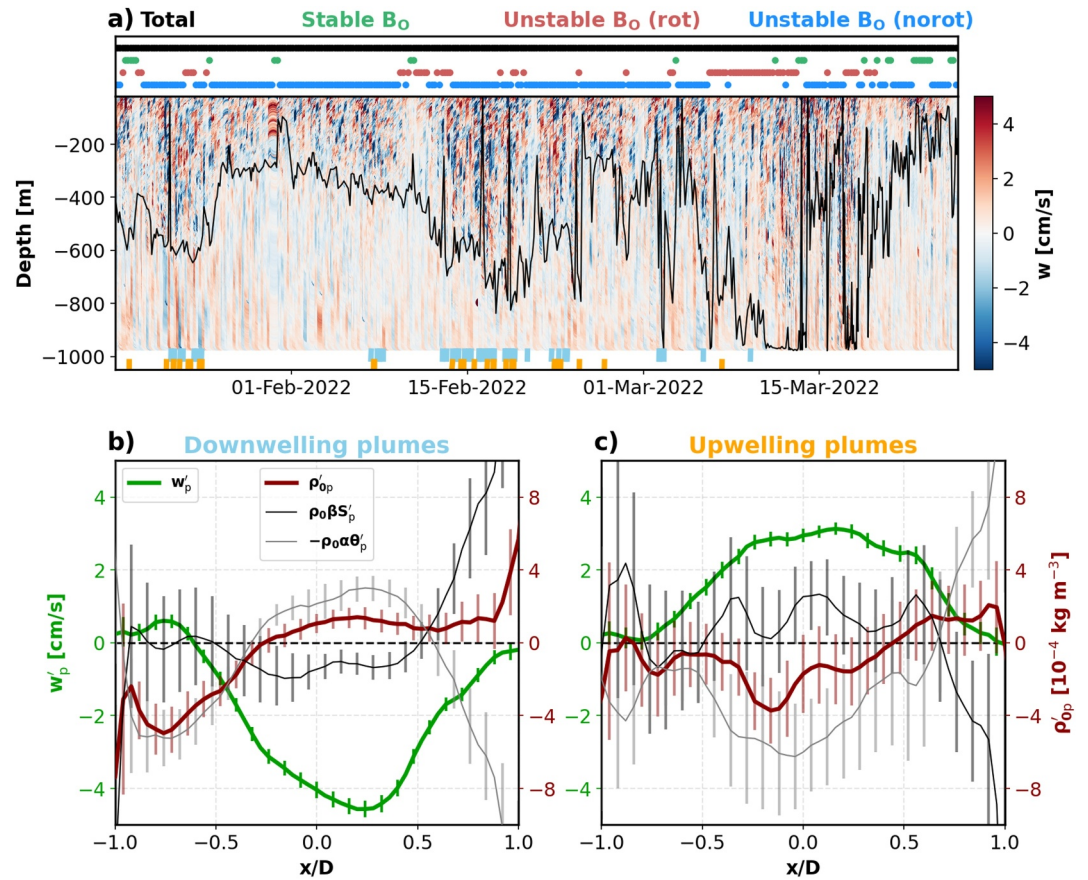


Figure 2. (a) Vertical velocity from glider 398 with the mixed-layer depth, h (black). The colored dots at the top indicate the periods used in (Figures 3c–3e). The dots at the bottom indicate periods of downwelling (blue) and upwelling (orange) plumes for the convective period before mid-March. Composite analysis of (b) downwelling and (c) upwelling plumes' vertical velocity (green), density (red), temperature (gray) and salinity (black) contributions to density anomalies displayed along the plume horizontal lengthscale non-dimensionalized by the plume diameter, x/D . Errorbars indicate standard error of the mean.

Rossby number is $Ro^* = (B_0/f^3h^2)^{1/2}$ with f the Coriolis parameter (Jones & Marshall, 1993). The mixed layer depth (MLD), h , is defined from a density threshold of 0.01 kg m^{-3} (Piron et al., 2016) and displayed in Figure S1 of Supporting Information S1 using a monthly density Argo climatology (Roemmich & Gilson, 2009). If the MLD is deeper than 1,000 m (0.2% of Pearldiver measurements), the MLD is set to 1,000 m to estimate z/h in Figures 3 and 4. B_0 is the surface buoyancy flux (Clément et al., 2023) estimated from the ERA5 reanalysis (Hersbach et al., 2020). Ro^* delimits the importance of rotation by separating non-rotational 3D turbulence from rotational quasi-2-D vortices, believed to form under the 3D turbulent layer under strong rotational control (Maxworthy & Narimousa, 1994; Pirro et al., 2022).

3. Results

3.1. Plume Detection

Individual convective plumes are first identified from w (Figure 2a and Figure S2 in Supporting Information S1). Then, the plume characteristics are defined from a composite analysis (Figures 2b and 2c) displayed along the plume horizontal lengthscale non-dimensionalized by the plume diameter, x/D , for convective periods until mid-March. Over the three winter glider deployments, 73 downwelling and 57 upwelling plumes were detected. These downwelling plumes have a composite horizontal length-scale (width) of $620 \pm 400 \text{ m}$ that is crossed in approximately one hour by the gliders. A 4-min averaged w is used to detect the plumes and their width, which is defined from the w zero-crossings. Note that the gliders do not necessarily cross a plume through its center, and so

the average plume diameter is likely higher than this value. Downwelling plume composites of vertical velocity and density show dense waters moving downwards (w'_p and ρ'_{0p} in Figure 2b, where subscript p indicates average over all plumes and prime denotes anomaly relative to the time-averaged property of each plume). This contrasts with non-breaking linear internal waves in a stratified ocean without vertical buoyancy flux and supports the identification of plumes. Subsequent to atmospheric cooling, dense plumes are colder and fresher than their environment, with temperature anomalies (rather than salinity) dominating the density anomaly (Figure 2b).

The characteristic velocity and density in a downwelling plume are $w'_p = -4.6 \text{ cm s}^{-1}$ and $\rho'_{0p} = 1.5 \times 10^{-4} \text{ kg m}^{-3}$, which gives $w'_p b'_p = 0.7 \times 10^{-7} \text{ m}^2 \text{ s}^{-3}$. The area of the convective region occupied by downwelling plumes, defined as the plume total length-scale divided by the distance covered by the gliders, is $a_p = 3\%$. The upwelling plume composite (Figure 2c) has a maximum speed of 3.2 cm s^{-1} and a length-scale of $780 \pm 690 \text{ m}$. Upwelling plumes are associated with warm and salty waters (Figure 2c) and with negative density anomaly of $\rho'_{0p} = -3.8 \times 10^{-4} \text{ kg m}^{-3}$ centered around $x/D = -0.15$. Upwelling plumes were sampled in $a_p = 2\%$ of the convective region. Using Equation 4 (Supporting Information S1), we estimate a total non-local buoyancy flux $a_p w'_p b'_p$ of $4.3 \times 10^{-9} \text{ m}^2 \text{ s}^{-3}$ for both downwelling and upwelling plumes. This estimate implies that the non-local transport only roughly contributes to a tenth of the calculated buoyancy flux depth-integrated within the ML ($38.5 \times 10^{-9} \text{ m}^2 \text{ s}^{-3}$ in Figure 4a). Using characteristic velocity and density for plumes slightly overestimates the total buoyancy flux although it might also be underestimated by $\sim 10\%$ – 20% due to the glider undersampling at $\sim 1 \text{ min}$ (McPhee, 1992). This contribution remains lower than the 80% – 90% found in convective atmospheric environments (Giordani et al., 2020; Siebesma & Cuijpers, 1995). The low contribution of the non-local to the total buoyancy flux might arise from an under-sampling of convective plumes and of a_p . The gliders mainly went back and forth between the convective region and the edge of the boundary currents (398 and 409 in Figure S1 of Supporting Information S1). In contrast, in the northwestern Mediterranean Sea, a_p roughly covered a third of the convective region (Margirier et al., 2017), a value that would bring better agreement between our non-local and total buoyancy flux. Further targeted deployments in the center of the Labrador Sea and other convective regions should help refine the estimate of a_p and its variability.

The histogram of w is slightly skewed, with larger negative than positive w for $|w| = 4\text{--}8 \text{ cm s}^{-1}$ during periods of strong surface buoyancy loss (Figure S3 in Supporting Information S1). This skewness is consistent with convection in the Mediterranean Sea where skewed histograms of w were previously found (Margirier et al., 2017; Merckelbach et al., 2010).

3.2. Vertical Velocity Scalings

In this section, we use the three gliders deployed (~ 3 months each) in a convective environment to examine how the standard deviation of vertical velocity (σ_w), a proxy for turbulence, relates to atmospheric forcing. In particular, we test scalings (Table 1) for the surface layer (SL, top 10% of the boundary layer) and mixed layer (ML, top 0%–80% of the boundary layer, BL) to assess the dominant controls on glider-observed vertical velocities during Labrador Sea deep convection. Although the BL contains the ML and the entrainment zone (Lombardo & Gregg, 1989), the BL is here approximated by the ML (Buckingham et al., 2019).

For the surface layer, we compute the non-dimensionalized turbulence, approximated by the standard deviation of vertical velocity over friction velocity σ_w/u_* and average these values in z/L coordinates, with z the depth and L the Obukhov length (Table 1). This allows us to test the dependence of turbulent velocities on Monin-Obukhov scaling (Supporting Information S1). In periods with stabilizing or destabilizing buoyancy forcing, the computed ratio $\overline{\sigma_w}/u_*$ agrees well with the theoretical prediction from SL scaling (Figures 3a and 3b, Table 1). This demonstrates that in the upper-layer of the ocean, vertical velocities are in strong agreement with scalings for wind- and buoyancy-driven turbulence. This agreement would suggest that surface waves and Langmuir circulations are not important contributors to $\overline{\sigma_w}$ in the region, confirming previous observations for the region (Zheng, 2023). However, some of these effects may be strongest in the near surface layer and thus missed as we have removed the top 20 m. Additionally, the effect of Langmuir turbulence might also be incorporated in u_* (Miller et al., 2024). In the weakly stabilizing case (Figure 3a), the turbulent eddy size is limited by stratification and $\overline{\sigma_w}/u_*$ is independent of z . In the unstable case (Figure 3b), $\overline{\sigma_w}/u_*$ increases with increasing atmospheric buoyancy loss (B_0) from $z/L > 0.1$ and follows the free convective regime for $z/L \gg 1$. For weaker buoyancy

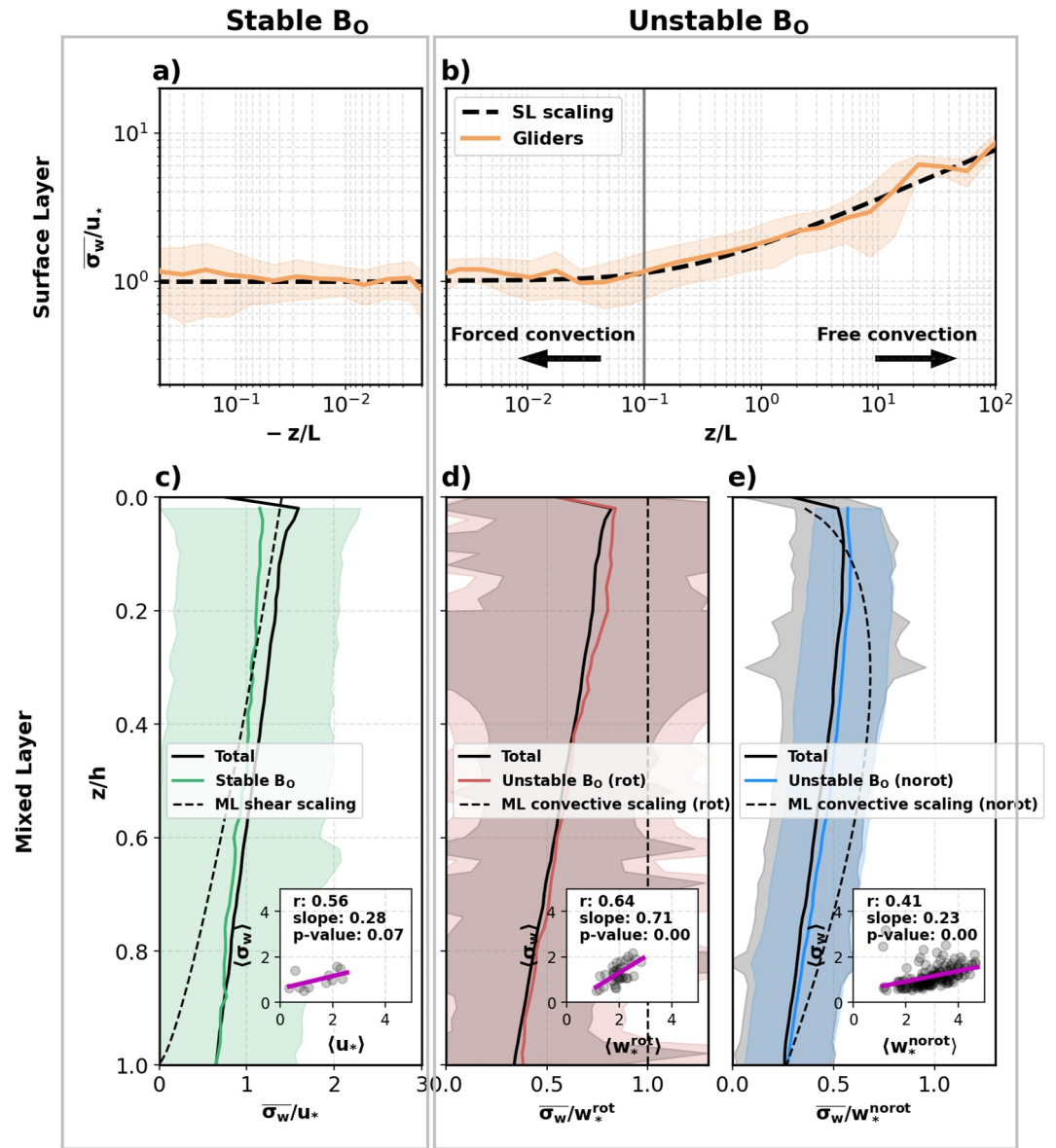


Figure 3. Surface (a, b) and mixed (c–e) layer scaling for the standard deviation of vertical velocity, σ_w . In (a, b), σ_w is plotted as a ratio over friction velocity, u_* , and averaged against z/L (orange). In (c, d), σ_w is bin-averaged against z/h with the mixed layer depth and plotted as a ratio against (c) u_* , (d) w_*^{rot} , the scaling for rotationally controlled convection and (e) w_*^{norot} , the scaling for non-rotationally-controlled convection. For each test, the calculation is averaged over all glider data (Total in black) or a subset corresponding to stable surface buoyancy forcing (c) in green, unstable surface buoyancy forcing and $Ro^* < 0.29$ in red (d) or $Ro^* > 0.29$ in blue (e). The small inset plots show the relationship between the 1-day average σ_w and the theoretical scaling along with their correlation coefficient (r), the slope of the regression, and the p-value. The theoretical scalings (Table 1) are shown in dashed black.

loss ($z/L < 0.1$), the forced convection regime approaches the stable regime with a constant $\overline{\sigma_w}/u_*$ (Figure 3b). Due to high surface heat loss in winter, the free convection regime covers 96% of the convective period, whereas the forced convection regime only occurs 4% of the time.

Within the mixed layer, the relationship between turbulent vertical velocity and scalings for shear-driven turbulence or rotationally controlled convection are tested. These scalings predict a vertical structure for the w standard deviation as a function of fractional depth in the mixed layer (z/h where h is the MLD). The black lines in Figures 3c–3e show each calculated ratio for all the glider data. Overall, the observed vertical velocities are relatively lower than the scalings for velocity (rotational and non-rotational convection in d and e, respectively).

Implied theoretical scalings are overlaid in dashed black which show that for shear driven ML, there is an expectation of stronger vertical velocities near the surface layer, and an agreement above $0.4z/h$ with the ratio selected under stable surface buoyancy forcing (green in Figure 3c).

For the scalings of vertical velocity during free convection (destabilizing buoyancy forcing), there exist two leading scalings for vertical velocities, depending on whether rotation is acting on and changing the character of the convective plume, or whether there are no rotational effects. Typically, one would expect that rotation is felt if the plume takes longer to descend to its neutral depth, so that there is time for rotation to be felt. The formal distinction used here is the natural Rossby number Ro^* , which is smaller for larger h . While this threshold varies in previous experiments from 0.03 (Coates & Ivey, 1997) to 1 (Jones & Marshall, 1993), here we use a threshold of $Ro^* = 0.29$ (Maxworthy & Narimousa, 1994) to separate the regimes (Text S1 in Supporting Information S1), where periods with a smaller Ro^* (larger mixed layer depth) are anticipated to correspond to rotationally controlled convection. From the glider data sets, 66% of the free convection periods are in the non-rotational regime ($Ro^* > 0.29$) and 34% are rotational ($Ro^* < 0.29$). For the calculation, $\bar{\sigma}_w$ is normalized by the rotational and non-rotational scalings for w (Table 1), and bin-averaged in z/h coordinate (Figures 3d and 3e). Nondimensionalized $\bar{\sigma}_w$ decays with depth regardless of the MLD and of the regime. Because of the rather constant winter surface buoyancy loss until mid-March with $B_0 = 0.9 \pm 0.5 \times 10^{-7} \text{ m}^2 \text{ s}^{-3}$, the distinction w_*^{norot} versus w_*^{rot} , or alternatively the MLD (Figure 2a) explains 78% of the variance of Ro^* using a multiple linear regression. Choosing free convective rotational or non-rotational periods, as opposed to the total period, does not meaningfully increase $\bar{\sigma}_w/w_*^{rot}$ or $\bar{\sigma}_w/w_*^{norot}$ to bring them closer to the ML convective scaling (dashed line in Figures 3d and 3e). One-day time-averaged comparisons (insets of Figures 3c–3e), however, favor rotating over non-rotating scaling during free convection with the highest correlation coefficient ($r = 0.64$) and slope of the regression (0.71). Due to the large uncertainties in the calculation, we note only that the scalings for rotating convection are a marginally better fit, whereas results from Lagrangian floats found a better agreement for non-rotating scalings in Labrador Sea convection (Steffen & D’Asaro, 2002).

3.3. Vertical Buoyancy Flux

Vertical buoyancy flux in the ocean occurs during deep convection; at the surface, buoyancy is lost to the atmosphere through cooling of the surface layer of the ocean. As this now denser water sinks, it carries relatively dense water downward ($w'b' > 0$ for $w' < 0$ and $b' < 0$), with the expectation of lighter water rising (also $w'b' > 0$). This is the situation observed during deep convection by the gliders (Figure 2), with dense plumes downwelling. Using the glider data, we can estimate the vertical profile of buoyancy flux, where the expectation is that the buoyancy flux near the surface matches the buoyancy flux from the ocean to the atmosphere (Harcourt et al., 2002), and near the mixed layer depth, the buoyancy flux goes to zero. If the buoyancy flux changes sign at/below the mixed layer depth, then this is referred to as “penetrative convection”, where instead of dense water going down, dense water is rising ($w'b' < 0$) and being entrained into the mixed layer.

During convection (mid-January to mid-March, approximately when $dh/dt < 0$), the vertical profile of buoyancy flux is mostly linear as a function of z/h (blue line in Figure 4a). Flux is positive near the surface and goes slightly negative at/below the mixed layer. During winter, the average air-sea buoyancy flux is $B_0 = 0.8 \times 10^{-7} \text{ m}^2 \text{ s}^{-3}$ (dashed black line in Figure 4a), which is in agreement with the near surface $\overline{w'b'}$ estimated from gliders. Separating the thermal and haline contributions to buoyancy flux (Figures 4b and 4c), we see—not unexpectedly due to the temperature decrease to the surface above $0.1z/h$ (red lines in Figures 4a and 4b)—that during convection the vertical buoyancy flux is primarily driven by temperature near the surface. In addition, entrainment of salty and warm water occurs from below the MLD (negative $-g\beta w'S'$ for $z/h > 0.6$, positive $gaw'\Theta'$ even below $z/h > 1.0$). The ratio of the buoyancy flux at the mixed layer base to that of the surface, defined as $n_* = -(\overline{w'b'})_h/B_0$, is 36%. In the atmosphere, this ratio is usually assumed to be smaller at 20% (Caughey & Palmer, 1979), which is used in boundary layer parameterization (Large et al., 1994; Reichl & Hallberg, 2018), although n_* may also contain contributions from wind stress in Figure 4a. Further studies in various convective environments will assess whether a spatially constant ratio is appropriate for oceanic parameterizations or whether the inclusion of wind stress and Langmuir turbulence is necessary (Q. Li & Fox-Kemper, 2017) in deep convective environments.

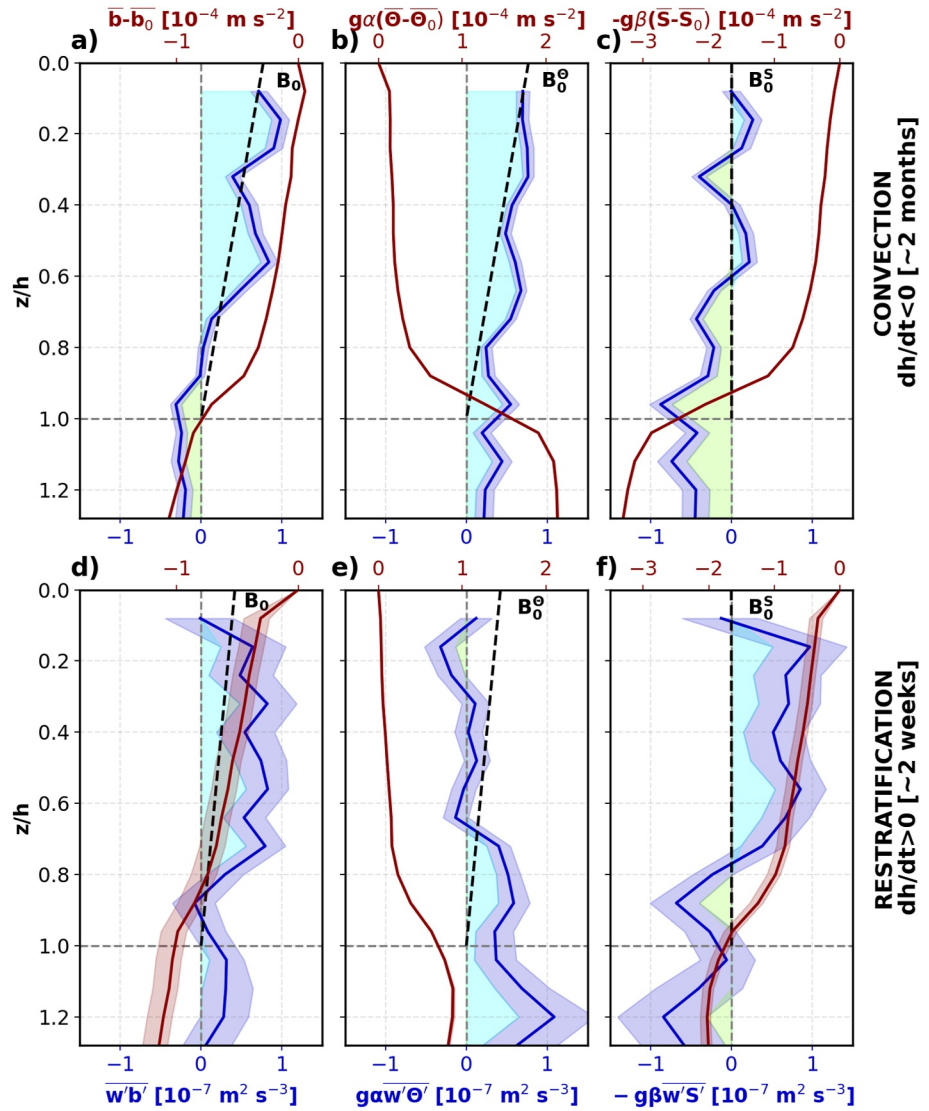


Figure 4. (a, d) Vertical buoyancy flux (blue, bottom x -axis) and buoyancy relative to its surface values b_0 (red, top x -axis) with their (b, e) temperature and (c, f) salinity contributions averaged over the convective (1st row) and restratifying (2nd row) periods. The buoyancy flux parameterization based on its surface value (B_0) decays linearly to zero (dashed black line) at the bottom of the mixed layer, h . Shading indicates the 95% bootstrap confidence intervals of the mean.

During restratification, the vertical convergence of buoyancy flux lightens shallow waters. Similar to the convective period, a positive buoyancy flux occurs during restratification in Figure 4d (last 2 weeks of March, approximately when $dh/dt > 0$), although driven by salinity (through $\overline{w'S'}$, Figure 4f). In the surface layer, buoyancy increases to the surface (Figure 4d) due to a freshwater input without temperature contribution (Figures 4e and 4f). The negligible atmospheric contribution to the buoyancy flux from the difference of evaporation and precipitation (B_0^S in Figure 4f) emphasizes the potential role of lateral freshwater fluxes for restratification (Clément et al., 2023; Straneo, 2006). Although submesoscale processes are expected to contribute to restratify the deep ML (Clément et al., 2023) and the decrease in buoyancy flux toward the surface (Figure 4d) resembles the contribution of frontal instabilities to $w'b'$ (Thomas et al., 2016), no link could be established between the lateral buoyancy gradient and $w'b'$. This absence of a link may result from insufficient high-resolution data or the overwhelming effect of convective buoyancy loss on $w'b'$.

As a secondary check to our estimates of the vertical buoyancy fluxes from gliders, we compare the evolution of seawater buoyancy (from temperature and salinity profiles) with the expected change due to the combination of

surface buoyancy fluxes (B_0) and the vertical flux near the mixed layer base ($w'b'_h$). Vertically integrating the buoyancy evolution equation gives $h\partial b/\partial t = w'b'_h - B_0$ (Reichl & Hallberg, 2018). During the convective period, the net buoyancy loss $h\partial b/\partial t$ is $-0.7 \times 10^{-7} \text{ m}^2 \text{ s}^{-3}$, estimated from the change in buoyancy between the start and end of the convective period and using $h = 450 \text{ m}$. Comparing this with the expected change due to the vertical flux at the MLD, we find $w'b'_h - B_0 = -1.1 \times 10^{-7} \text{ m}^2 \text{ s}^{-3}$, using the average values for $w'b'_h$ and B_0 from Figure 4a. If we evaluate the buoyancy evolution during the restratification period, the situation is more complicated due to a highly variable MLD and its overall shoaling (Figure 2a). During this period, the balance roughly holds over the upper portion of the mixed layer (top 70%) with the buoyancy convergence of $0.42 \times 10^{-7} \text{ m}^2 \text{ s}^{-3}$ (using $B_0 = 0.37 \times 10^{-7} \text{ m}^2 \text{ s}^{-3}$ and $w'b'_h = 0.79 \times 10^{-7} \text{ m}^2 \text{ s}^{-3}$ at $z/h = 0.7$ from Figure 4d) that balances the added buoyancy sampled independently by the gliders $h\partial b/\partial t = 0.35 \times 10^{-7} \text{ m}^2 \text{ s}^{-3}$. This agreement, and the stronger subsurface than surface buoyancy flux, imply a subsurface source of buoyancy, for example, from freshwater via lateral oceanic processes. This contrasts with the dominant loss of buoyancy at the surface due to heat loss to the atmosphere during the convective period.

4. Conclusions

Three gliders provided vertical water velocity measurements every minute for 3 months within the top 1,000 m of the central Labrador Sea, including during wintertime deep convection. Using these velocity measurements, we find that:

- Downwelling convective plumes have a length scale of 620 m, a vertical velocity magnitude up to 4.6 cm s^{-1} , and cover roughly 3% of the convective region. The vertical velocities have a slightly skewed distribution (Figure S3 in Supporting Information S1)—that is, they show narrower and faster downwelling plumes compared to upwelling.
- Vertical velocity variance in the surface layer is controlled by wind- and convectively driven turbulence, while in the ocean boundary layer it shows marginally better agreement with theoretical rotational scalings than with non-rotational control.
- The vertical profile of buoyancy flux is positive at the surface during both convection and restratification, and negative at the mixed layer base during convection. During convection, the buoyancy flux is dominated by heat flux and matches the surface buoyancy loss, while the change in sign of buoyancy flux at the mixed layer base is indicative of entrainment from below/penetrative convection. During restratification, salt/freshwater flux dominates (a downward flux of salty water/upward flux of freshwater).

Overall these vertical velocity measurements enabled identification of kilometer-scale downward convective plumes of cold water in the Labrador Sea. The measurements of vertical velocity were used to estimate vertical buoyancy flux, including distinguishing between heat and freshwater fluxes at different stages of convection. These methods offer a promising approach for comparing oceanic convective environments sampled by gliders and for evaluating convection in ocean models. These methods could also be extended to estimate vertical fluxes of biogeochemical properties (Omand et al., 2015) such as oxygen or carbon.

Data Availability Statement

The data sets for 398/409 and PearlDiver are available on SEANOE from Clément and Frajka-Williams (2021) and von Oppeln-Bronikowski et al. (2022), respectively.

References

- Buckingham, C. E., Lucas, N. S., Belcher, S. E., Rippeth, T. P., Grant, A. L. M., Sommer, J. L., et al. (2019). The contribution of surface and submesoscale processes to turbulence in the open ocean surface boundary layer. *Journal of Advances in Modeling Earth Systems*, 11(12), 4066–4094. <https://doi.org/10.1029/2019MS001801>
- Businger, J. A., Wyngaard, J. C., Izumi, Y., & Bradley, E. F. (1971). Flux-profile relationships in the atmospheric surface layer. *Journal of the Atmospheric Sciences*, 28(2), 181–189. [https://doi.org/10.1175/1520-0469\(1971\)028<0181:fprita>2.0.co;2](https://doi.org/10.1175/1520-0469(1971)028<0181:fprita>2.0.co;2)
- Caughey, S. J., & Palmer, S. G. (1979). Some aspects of turbulence structure through the depth of the convective boundary layer. *Quarterly Journal of the Royal Meteorological Society*, 105(446), 811–827. <https://doi.org/10.1002/qj.49710544606>
- Clément, L., & Frajka-Williams, E. (2021). TERIFIC 2nd ocean glider deployments in the Labrador Sea [Dataset]. *SEANOE*. <https://doi.org/10.17882/101369>
- Clément, L., Frajka-Williams, E., Von Oppeln-Bronikowski, N., Goszczko, I., & de Young, B. (2023). Cessation of Labrador Sea convection triggered by distinct fresh and warm (sub) mesoscale flows. *Journal of Physical Oceanography*, 53, 1959–1977. <https://doi.org/10.1175/JPO-D-22-0178.1>

Acknowledgments

L. Clément and E. Frajka-Williams were supported by TERIFIC, which is funded by the European Research Council (ERC) under the European Union's Horizon 2020 research and innovation programme (Grant Agreement 803140). The authors would like to thank Dr. I. Giddy and an anonymous reviewer for their helpful comments, which helped improve this manuscript. This study also benefited from discussions with Dr. B. Gülk.

- Coates, M., & Ivey, G. (1997). On convective turbulence and the influence of rotation. *Dynamics of Atmospheres and Oceans*, 25(4), 217–232. [https://doi.org/10.1016/S0377-0265\(96\)00479-4](https://doi.org/10.1016/S0377-0265(96)00479-4)
- D'Asaro, E. A. (2001). Turbulent vertical kinetic energy in the ocean mixed layer. *Journal of Physical Oceanography*, 31(12), 3530–3537. [https://doi.org/10.1175/1520-0485\(2002\)031<3530:TVKEIT>2.0.CO;2](https://doi.org/10.1175/1520-0485(2002)031<3530:TVKEIT>2.0.CO;2)
- Frajka-Williams, E., Eriksen, C. C., Rhines, P. B., & Harcourt, R. R. (2011). Determining vertical water velocities from Seaglider. *Journal of Atmospheric and Oceanic Technology*, 28(12), 1641–1656. <https://doi.org/10.1175/2011JTECH0830.1>
- Gascard, J. C., & Clarke, R. A. (1983). The formation of Labrador Sea water. Part II: Mesoscale and smaller-scale processes. *Journal of Physical Oceanography*, 13(10), 1779–1797. [https://doi.org/10.1175/1520-0485\(1983\)013<1779:TFOLSW>2.0.CO;2](https://doi.org/10.1175/1520-0485(1983)013<1779:TFOLSW>2.0.CO;2)
- Gelderloos, R., Katsman, C. A., & Drijfhout, S. S. (2011). Assessing the roles of three eddy types in restratifying the Labrador Sea after deep convection. *Journal of Physical Oceanography*, 41(11), 2102–2119. <https://doi.org/10.1175/JPO-D-11-054.1>
- Giordani, H., Bourdallé-Badie, R., & Madec, G. (2020). An eddy-diffusivity mass-flux parameterization for modeling oceanic convection. *Journal of Advances in Modeling Earth Systems*, 12(9). <https://doi.org/10.1029/2020MS002078>
- Harcourt, R. R., Steffen, E. L., Garwood, R. W., & D'Asaro, E. A. (2002). Fully Lagrangian floats in Labrador Sea deep convection: Comparison of numerical and experimental results. *Journal of Physical Oceanography*, 32(2), 493–509. [https://doi.org/10.1175/1520-0485\(2002\)032<0493:FLFILS>2.0.CO;2](https://doi.org/10.1175/1520-0485(2002)032<0493:FLFILS>2.0.CO;2)
- Hayes, D., & Morison, J. (2002). Determining turbulent vertical velocity, and fluxes of heat and salt with an autonomous underwater vehicle. *Journal of Atmospheric and Oceanic Technology*, 19(5), 759–779. [https://doi.org/10.1175/1520-0426\(2002\)019<0759:DTVVA>2.0.CO;2](https://doi.org/10.1175/1520-0426(2002)019<0759:DTVVA>2.0.CO;2)
- Hersbach, H., Bell, B., Berrisford, P., Hirahara, S., Horányi, A., Muñoz-Sabater, J., et al. (2020). The ERA5 global reanalysis. *Quart. J. Roy. Meteor. Soc.*, 146(730), 1999–2049. <https://doi.org/10.1002/qj.3803>
- Jones, H., & Marshall, J. (1993). Convection with rotation in a neutral ocean: A study of open-ocean deep convection. *Journal of Physical Oceanography*, 23(6), 1009–1039. [https://doi.org/10.1175/1520-0485\(1993\)023<1009:CWRIAN>2.0.CO;2](https://doi.org/10.1175/1520-0485(1993)023<1009:CWRIAN>2.0.CO;2)
- Large, W. G., McWilliams, J. C., & Doney, S. C. (1994). Oceanic vertical mixing: A review and a model with a nonlocal boundary layer parameterization. *Reviews of Geophysics*, 32(4), 363–403. <https://doi.org/10.1029/94RG01872>
- Lenschow, D. H., Wyngaard, J. C., & Pennell, W. T. (1980). Mean-field and second-moment budgets in a baroclinic, convective boundary layer. *Journal of the Atmospheric Sciences*, 37(6), 1313–1326. [https://doi.org/10.1175/1520-0469\(1980\)037<1313:MFASMB>2.0.CO;2](https://doi.org/10.1175/1520-0469(1980)037<1313:MFASMB>2.0.CO;2)
- Li, F., Lozier, M. S., Danabasoglu, G., Holliday, N. P., Kwon, Y.-O., Romanou, A., et al. (2019). Local and downstream relationships between Labrador Sea water volume and North Atlantic meridional overturning circulation variability. *Journal of Climate*, 32(13), 3883–3898. <https://doi.org/10.1175/JCLI-D-18-0735.1>
- Li, Q., & Fox-Kemper, B. (2017). Assessing the effects of Langmuir turbulence on the entrainment buoyancy flux in the ocean surface boundary layer. *Journal of Physical Oceanography*, 47(12), 2863–2886. <https://doi.org/10.1175/JPO-D-17-0085.1>
- Lilly, J. M., Rhines, P. B., Schott, F., Lavender, K., Lazier, J., Send, U., & D'Asaro, E. (2003). Observations of the Labrador Sea eddy field. *Progress in Oceanography*, 59(1), 75–176. <https://doi.org/10.1016/j.pocean.2003.08.013>
- Lombardo, C. P., & Gregg, M. C. (1989). Similarity scaling of viscous and thermal dissipation in a convecting surface boundary layer. *Journal of Geophysical Research*, 94(C5), 6273–6284. <https://doi.org/10.1029/jc094ic05p06273>
- Margirier, F., Bosse, A., Testor, P., L'Hévéder, B., Mortier, L., & Smeed, D. (2017). Characterization of convective plumes associated with oceanic deep convection in the northwestern Mediterranean from high-resolution in situ data collected by gliders. *Journal of Geophysical Research: Oceans*, 122(12), 9814–9826. <https://doi.org/10.1002/2016JC012633>
- Maxworthy, T., & Narimousa, S. (1994). Unsteady, turbulent convection into a homogeneous, rotating fluid, with oceanographic applications. *Journal of Physical Oceanography*, 24(5), 865–887. [https://doi.org/10.1175/1520-0485\(1994\)024<0865:UTCIAH>2.0.CO;2](https://doi.org/10.1175/1520-0485(1994)024<0865:UTCIAH>2.0.CO;2)
- McPhee, M. G. (1992). Turbulent heat flux in the upper ocean under sea ice. *Journal of Geophysical Research*, 97(C4), 5365–5379. <https://doi.org/10.1029/92JC00239>
- Merckelbach, L., & Carpenter, J. R. (2021). Ocean glider flight in the presence of surface waves. *Journal of Atmospheric and Oceanic Technology*, 38, 1265–1275. <https://doi.org/10.1175/jtech-d-20-0206.1>
- Merckelbach, L., Smeed, D., & Griffiths, G. (2010). Vertical water velocities from underwater gliders. *Journal of Atmospheric and Oceanic Technology*, 27(3), 547–563. <https://doi.org/10.1175/2009JTECH0710.1>
- Miller, U. K., Zappa, C. J., Zippel, S. F., Farrar, J. T., & Weller, R. A. (2024). Scaling of moored surface ocean turbulence measurements in the Southeast Pacific Ocean. *Journal of Geophysical Research: Oceans*, 128(1). <https://doi.org/10.1029/2022JC018901>
- Mironov, D. V., Gryanik, V. M., Moeng, C. H., Olbers, D. J., & Warnecke, T. H. (2000). Vertical turbulence structure and second-moment budgets in convection with rotation: A large-eddy simulation study. *Quarterly Journal of the Royal Meteorological Society*, 126(563), 477–515. <https://doi.org/10.1002/qj.49712656306>
- Nieuwstadt, F. T. M. (1984). The turbulent structure of the stable, nocturnal boundary layer. *Journal of the Atmospheric Sciences*, 41(14), 2202–2216. [https://doi.org/10.1175/1520-0469\(1984\)041<2202:tsots>2.0.co;2](https://doi.org/10.1175/1520-0469(1984)041<2202:tsots>2.0.co;2)
- Niiler, P. P., & Krauss, E. B. (1977). One-dimensional models of the upper ocean. In E. B. Kraus (Ed.), *Modelling and prediction of the upper layers of the ocean* (pp. 143–172). Pergamon Press.
- Omand, M., D'Asaro, E. A., Lee, C. M., Perry, M. J., Briggs, N., Cetinić, I., & Mahadevan, A. (2015). Eddy-driven subduction exports particulate organic carbon from the spring bloom. *Science*, 348(6231), 222–225. <https://doi.org/10.1126/science.1260062>
- Piron, A., Thierry, V., Mercier, H., & Caniaux, G. (2016). Argo float observations of basin-scale deep convection in the Irminger Sea during winter 2011–2012. *Deep-Sea Research. Part. I*, 109, 76–90. <https://doi.org/10.1016/j.dsr.2015.12.012>
- Pirro, A., Mauri, E., Gerin, R., Martellucci, R., Zuppelli, P., & Poulain, P. M. (2022). New insights on the formation and breaking mechanism of convective cyclonic cones in the South Adriatic Pit during winter 2018. *Journal of Physical Oceanography*, 52(9), 2049–2068. <https://doi.org/10.1175/JPO-D-21-0108.1>
- Reichl, B. G., & Hallberg, R. (2018). A simplified energetics based Planetary Boundary Layer (ePBL) approach for ocean climate simulations. *Ocean Modelling*, 132, 112–129. <https://doi.org/10.1016/j.ocemod.2018.10.004>
- Roemmich, D., & Gilson, J. (2009). The 2004–2008 mean and annual cycle of temperature, salinity, and steric height in the global ocean from the Argo Program. *Progress in Oceanography*, 82(2), 81–100. <https://doi.org/10.1016/j.pocean.2009.03.004>
- Rykova, T., Straneo, F., Lilly, J., & Yashayaev, I. (2009). Irminger Current anticyclones in the Labrador Sea observed in the hydrographic record, 1990–2004. *Journal of Marine Research*, 67(3), 361–384. <https://doi.org/10.1357/002224009789954739>
- Schott, F., Visbeck, M., Send, U., Fischer, J., Stramma, L., & Desaubies, Y. (1996). Observations of deep convection in the Gulf of Lions, northern Mediterranean, during the winter of 1991/92. *Journal of Physical Oceanography*, 26(4), 505–524. [https://doi.org/10.1175/1520-0485\(1996\)026<0505:OODCIT>2.0.CO;2](https://doi.org/10.1175/1520-0485(1996)026<0505:OODCIT>2.0.CO;2)
- Siebesma, A. P., & Cuijpers, J. W. M. (1995). Evaluation of parametric assumptions for shallow cumulus convection. *Journal of the Atmospheric Sciences*, 52(6), 650–666. [https://doi.org/10.1175/1520-0469\(1995\)052<0650:EOPAFS>2.0.CO;2](https://doi.org/10.1175/1520-0469(1995)052<0650:EOPAFS>2.0.CO;2)

- Siebesma, A. P., Soares, P. M. M., & Teixeira, J. (2007). A combined eddy-diffusivity mass-flux approach for the convective boundary layer. *Journal of the Atmospheric Sciences*, *64*(4), 1230–1248. <https://doi.org/10.1175/JAS3888.1>
- Steffen, E. L., & D'Asaro, E. A. (2002). Deep convection in the Labrador Sea as observed by Lagrangian floats. *Journal of Physical Oceanography*, *32*(2), 475–492. [https://doi.org/10.1175/1520-0485\(2002\)032<0475:DCITLS>2.0.CO;2](https://doi.org/10.1175/1520-0485(2002)032<0475:DCITLS>2.0.CO;2)
- Straneo, F. (2006). Heat and freshwater transport through the central Labrador Sea. *Journal of Physical Oceanography*, *36*(4), 606–628. <https://doi.org/10.1175/JPO2875.1>
- Stull, R. B. (1976). The energetics of entrainment across a density interface. *Journal of the Atmospheric Sciences*, *33*, 1260–1267. [https://doi.org/10.1175/1520-0469\(1976\)033<1260:TEOEAD>2.0.CO;2](https://doi.org/10.1175/1520-0469(1976)033<1260:TEOEAD>2.0.CO;2)
- Thomas, L. N., Taylor, J. R., D'Asaro, E. A., Lee, C. M., Klymak, J. M., & Shcherbina, A. (2016). Symmetric instability, inertial oscillations, and turbulence at the Gulf Stream front. *Journal of Physical Oceanography*, *46*(1), 197–217. <https://doi.org/10.1175/JPO-D-15-0008.1>
- von Oppeln-Bronikowski, N., de Young, B., Bachmayer, R., Palter, J., Claus, B., Zhou, M., et al. (2022). Memorial University ocean glider deployments [Dataset]. *SEANOE*. <https://doi.org/10.17882/79349>
- Wilson, J. D. (2008). Monin-Obukhov functions for standard deviations of velocity. *Boundary-Layer Meteorology*, *129*(3), 353–369. <https://doi.org/10.1007/s10546-008-9319-5>
- Wyngaard, J. C., Coté, O. R., & Izumi, Y. (1971). Local free convection, similarity, and the budgets of shear stress and heat flux. *Journal of the Atmospheric Sciences*, *28*(7), 1171–1182. [https://doi.org/10.1175/1520-0469\(1971\)028<1171:LFCSAT>2.0.CO;2](https://doi.org/10.1175/1520-0469(1971)028<1171:LFCSAT>2.0.CO;2)
- Zheng, Z. (2023). *Impacts of surface waves on turbulence in ocean surface boundary layers: Observations and scaling*. University of Washington, PhD thesis.